International Journal of Multiphase Flow 118 (2019) 87–96

Contents lists available at ScienceDirect

International Journal of Multiphase Flow

journal homepage: www.elsevier.com/locate/ijmulflow

Dispersion of stratified dust layers by a moving shock wave

Shuyue Lai[a,*], Ryan W. Houim[b], Elaine S. Oran[a]

[a] Department of Aerospace Engineering, University of Maryland, College Park, MD, 20742, United States
[b] Department of Mechanical and Aerospace Engineering, University of Florida, Gainesville, FL, 32611, United States

ARTICLE INFO

Article history:
Received 23 January 2019
Revised 2 May 2019
Accepted 6 June 2019
Available online 11 June 2019

Keywords:
Shock-dust interaction
Granular flow
Segregation

ABSTRACT

Simulations of a shock passing over stratified dust layers containing two different types of particles were conducted to explore the effect of particle size and dust layer thickness on particle dispersion with application to coal mine explosion conditions. The simulations solve the Euler equations of fluid dynamics and granular flow, and accounts for different particle types using a binning approach. Test cases with a 2.7-mm layer consisting of particles with a smaller diameter ($d_{s,2}$=10, 20, and 40 μm) placed on top of a 10-mm layer consisting particles with a larger diameter ($d_{s,1}$=80 μm) were performed to study the effect of particle size on dust dispersion. The results indicate that larger particles from the lower layer can be lifted higher than the smaller particles from the upper layer if the two types of particles have a large size difference. In addition, dust dispersion of a shock passing over a rock-dust layer on top of a coal-dust layer were also investigated. Here the coal dust has a diameter of 30 μm and a density of 1330 kg/m^3, and the rock dust has a diameter of 15 μm and a density of 2680 kg/m^3. The rock-layer thickness of 1, 2, and 3 mm were considered, and the coal-dust layer underneath had a thickness of 4 mm. The results suggest that the rock particles work more effectively on suppressing the coal dust from lifting with increasing rock-layer thickness. Placing another layer of coal dust on top of the rock-coal layer shows that the rock dust underneath fails to suppress the coal particles above from being lifted, and this suggests the need to simultaneously or regularly apply rock dust during the mining operation.

1. Introduction

Dust explosions have been a serious industrial hazard for centuries in underground coal mines. Usually, an initial explosion of natural gas generates shock waves that propagate through the mine channels. These shock waves interact with and disperse layers of coal dust, which can then ignite in the hot, compressed environment. Ignition of dispersed coal particles may then lead to a secondary explosion, which can be more destructive than a primary one (Fletcher, 1976; Hwang, 1986). Therefore, understanding how the dust cloud forms due to the propagating shock wave, and identifying the important and controlling parameters of the flow, will provide important information that can be used to determine how to prevent and mitigate a dust explosion.

In the past, laboratory experiments and computations have been carried out to quantify and explain the lifting mechanism of a dust layer by a shock wave. Gerrard (1963) performed the first experimental work on dust lifting behind a moving shock. He concluded that particles were lifted due to the reflection of pressure waves and shock waves from the bottom of the channel. Borisov et al. (1967) concluded through similar experiments that dust was lifted by surface instabilities that developed due to the compression and reflected compression waves, which bounced back and forth between the chamber wall and the dust surface. These conclusions were later criticized by Fletcher (1976) based on both experimental and numerical investigations. Fletcher believed that dust was lifted due to instabilities induced by the rapid flow behind the shock wave instead of the reflecting compression wave. More recently, Houim et al. (2016) and Ugarte et al. (2017) identified the governing forces responsible for dust dispersion through numerical simulations. They found that the dust dispersion was initiated by the intergranular force between the particles. In addition, Magnus lift force and drag force were found to have significant effects at later stages (Ugarte et al., 2017).

An important parameter in the dispersion process is the size of the dispersing particles. Both experimental and numerical analyses have shown that particles with different sizes and densities can be dispersed into different heights. Nevertheless, contradictory observations have been reported. The numerical studies by Hwang (1986) and Ugarte et al. (2017) found that larger particles were lifted higher than smaller particles, while the experiments by Suzuki and Adachi (1984) and the simulations by

* Corresponding author.
E-mail addresses: lsy0830@umd.com, lsy0830@umd.edu (S. Lai).

https://doi.org/10.1016/j.ijmultiphaseflow.2019.06.008
0301-9322/

Zhu et al. (2012) observed the opposite trend. These contradictions could be due to the inconsistency in time and length scales or controlled variables among different studies. In addition, the agglomeration effect of the particles during experiments made it hard to determine the effective particle sizes (Ugarte et al., 2017).

All of the studies summarized above assumed a single particle type within the dust layer. In actual underground coal mines, however, rock dust is usually applied for inerting and suppressing of coal-dust dispersion and ignition. In fact, it is required by MSHA (Mine Safety and Health Administration) that the total incombustible content (TIC) is at least 80% when mixed with coal to prevent dust explosions (Luo et al., 2017). Therefore, the dust layer in coal mines consists of both rock and coal particles, which are usually different in size and density, and thus form a polydispersed granular system. Ideally, the rock dust, which is applied regularly to the dust surfaces during the mining operation, would suppress the dispersion of the coal dust underneath. In addition, a coal-rock mixture would be formed in the dispersed gas due to disturbances. The rock dust, then would act as a thermal inhibitor and prevent flame propagation (Man and Teacoach, 2009). In actual situations, a propagating shock wave could separate the rock and coal particles according to their different sizes and densities, and destroy the well-mixed rock-coal mixture. The ignition of the separated coal dust could still lead to a secondary explosion. Therefore, studying the dispersion of a dust layer containing different particle types and their segregation phenomenon is important to ensure safety in coal mines.

Very limited experimental or numerical studies have focused on dust lifting in a polydispersed system (i.e., a dust layer containing nonuniform particle sizes and densities). Chowdhury et al. (2018) made the first attempt to measure the effect of size polydispersity in a dust layer behind a moving shock wave. Their experimental findings concluded that dust entrainment decreases as the particle size increases, and a sample containing a wider range of size distribution (i.e., high polydipsersity) lifts higher than a sample with the same mean size, but lower polydipsersity (Chowdhury et al., 2018).

Recently, we have studied the effects of particle size and density in a polydispersed dust layer with a Eulerian-Eulerian multifluid granular model (Lai et al., 2018). Our results showed that particles with greater size and smaller density are lifted higher than particles with smaller size and greater density when the different types of particles were originally well mixed. Larger and lighter particles experience a greater Magnus lift force that pull particles upwards, and were opposed by a smaller drag force pushing the particles to the downwards (Lai et al., 2018).

In this paper, we continue the study of dust dispersion in polydispersed systems behind a moving shock wave. Here, instead of studying a single dust layer containing uniformly mixed particle types, the focus has shifted to the more realistic configurations, where a shock wave passes over multiple dust layers containing either coal or rock particles (stratified layer). This investigation is done to provide a qualitative understanding of the dispersion process of a stratified dust layer and the effect of particle size and dust-layer thickness on the results.

The model used in this research is an extension of the Eulerian-Eulerian granular model proposed by Houim and Oran (2016). In this model, the constitutive relations for the particle phases are derived from the Kinetic Theory of Granular Flow (KTGF). Multiple particle types are considered through a binning approach to study particle segregation (Lai et al., 2018). Particles in each bin have their own uniform particle size and diameter, and each bin of particles adds an additional set of governing equations and can have different properties. As a result, this model involves solving (M+1) sets of coupled Euler equations, one for the gas phase, and M indicates M different particle phases.

For simulating granular flows, the two most frequently used models are Eulerian-Eulerian, and Eulerian-Lagrangian models. In the Eulerian-Lagrangian approach, the particles are treated as discrete entities that are tracked individually. In the Eulerian-Eulerian approach, the particle phase is modeled as a continuum and the governing equations for a continuous, compressible media is solved. The Eulerian-Lagrangian approach can capture the physical behavior of the granular flow more accurately than a continuum description. Nevertheless, for a realistic problem, the number of Lagrangian particles can become extremely large, and so that it becomes computationally prohibitive for the calculations in dense regimes. Therefore, the Eulerian-Eulerian approach is used here so that large-scale simulations can be done at a resonable computational cost. One major issue for an Eulerian-Eulerian model is that it becomes invalid in very dilute particle regimes, where there are too few particles within each computational cell.

2. Physical and numerical model

Fig. 1 shows the initial and boundary conditions for the simulations. The two-dimensional channel is 10.2 cm high and 7 m in length. A Mach 1.4 shock placed at $x_{\text{shock}} = 5$ cm is propagating over two dust layers that consist of either particle type I or II. The background temperature (T_0) and pressure (P_0) is 295 K and 67 kPa, respectively. (These initial conditions are based on the experiments performed by Chowdhury et al. (2015)). The post-shock condition is determined by the Rankine-Hugoniot relations. The left and right side of the channel are non-reflecting, inflow-outflow boundary conditions and the top and bottom side of the domain are symmetry planes. The gas is assumed to be air. Both types of particles have an initial volume fraction (α_s) of 0.47, and a coefficient of restitution, e, of 0.9.

2.1. Governing equations

The details of the equations that describe a compressible multifluid granular gas can be found in Lai et al. (2018). The model is extended based on the work of Houim and Oran (2016), and now allows different particle sizes and densities with a binning approach. Each bin of particles has the same size and density. Including each specific type of particles requires adding a new set of governing equations that are coupled with the gas phase as well as all the other particle types. Effects of granular energy exchange between different particle bins, the dissipation of granular energy due to inelastic collisions between different particle bins, the granular viscous stress terms, and phase changes are neglected (Lai et al., 2018). In addition, the gas and dust considered in this model are assumed to be nonreactive.

The three governing equations for the gas phase are:

$$\frac{\partial \alpha_g \rho_g}{\partial t} + \boldsymbol{\nabla}\cdot(\alpha_g \rho_g \boldsymbol{v}_g) = 0, \tag{1}$$

$$\frac{\partial \alpha_g \rho_g \boldsymbol{v}_g}{\partial t} + \boldsymbol{\nabla}\cdot(\alpha_g \rho_g \boldsymbol{v}_g \boldsymbol{v}_g) = -\alpha_g \nabla p_g + \alpha_g \rho_g \boldsymbol{g} + \boldsymbol{S}_g^p, \tag{2}$$

$$\frac{\partial \alpha_g \rho_g E_g}{\partial t} + \boldsymbol{\nabla}\cdot[\alpha_g \boldsymbol{v}_g(\rho_g E_g + p_g)] = -p_{int}\sum_{m=1}^{M} \boldsymbol{\nabla}\cdot(\alpha_{s,m}\boldsymbol{v}_{s,m}) + \alpha_g \rho_g \boldsymbol{g}\cdot\boldsymbol{v}_g + S_g^E. \tag{3}$$

The four governing equations for particle type l are

$$\frac{\partial \alpha_{s,l} \rho_{s,l}}{\partial t} + \boldsymbol{\nabla}\cdot(\alpha_{s,l} \rho_{s,l} \boldsymbol{v}_{s,l}) = 0, \tag{4}$$

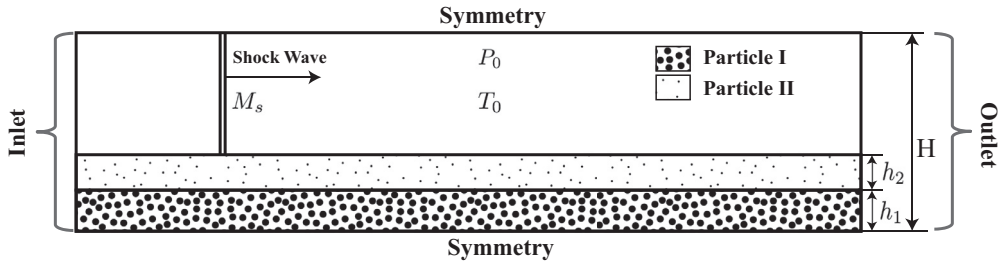

Fig. 1. Schematic diagram of the initial conditions for the two-dimensional siumlations where a shock of strength M_s travels over two dust layers. A dust layer containing particle type I of thickness and h_1 lies underneath a dust layer containing particley type II of thickness h_2.

$$\frac{\partial \alpha_{s,l}\rho_{s,l}\boldsymbol{v}_{s,l}}{\partial t} + \boldsymbol{\nabla}\cdot(\alpha_{s,l}\rho_{s,l}\boldsymbol{v}_{s,l}\boldsymbol{v}_{s,l}) + \boldsymbol{\nabla}p_{sl,\mathrm{tot}} = -\alpha_{s,l}\boldsymbol{\nabla}p_g + \alpha_{s,l}\rho_{s,l}\boldsymbol{g} - \boldsymbol{S}^p_{s,l}, \quad (5)$$

$$\frac{\partial \alpha_{s,l}\rho_s E_{s,l}}{\partial t} + \boldsymbol{\nabla}\cdot(\alpha_{s,l}\rho_{s,l}E_{s,l}\boldsymbol{v}_{s,l}) = -p_{s,l}\boldsymbol{\nabla}\cdot\boldsymbol{v}_{s,l} + S^{PTE}_{s,l}, \quad (6)$$

$$\frac{\partial \alpha_{s,l}\rho_{s,l}e_{s,l}}{\partial t} + \boldsymbol{\nabla}\cdot(\alpha_{s,l}\rho_{s,l}e_{s,l}\boldsymbol{v}_{s,l}) = S^E_{s,l}. \quad (7)$$

In these equations, subscripts g and s refer to the gas and the solid phase, respectively. Subscripts l indicates any particle type in the granular system. Here α, ρ, v and p represent the volume fraction, density, velocity, and pressure of the gas or the particular particle phase. Also, E_g, e_s, and E_s represent the gas-phase total energy, the particle internal energy, and the pseudo-thermal energy (PTE, i.e., the energy due to random translational motion of particles (Houim and Oran, 2016)). The interphase coupling terms describeing transfer of momentum and energy between the gas and the particle phases are denoted by $\boldsymbol{S}^p_g$, S^E_g, $\boldsymbol{S}^p_{s,l}$, $S^{PTE}_{s,l}$, and $S^E_{s,l}$.

The ideal-gas equation-of-state is used for the gas phase. The solids pressure $p_{s,l}$ takes into account the collisional effect of the particles and is defined as Huilin et al. (2003),

$$P_{s,l} = \alpha_{s,l}\rho_{s,l}\Theta_{s,l} + \sum_{m=1}^{M} P_{c,lm}. \quad (8)$$

Here $P_{c,lm}$ is the collisional part of the pressure between particle type l and m Huilin et al. (2003), and $\alpha_{s,l}\rho_{s,l}\Theta_{s,l}$ is the kinetic term for particle type l.

The total intergranular stress is defined as the sum of the solids and friction pressure for each particle type,

$$P_{sl,tot} = P_{s,l} + P_{fric,l}. \quad (9)$$

The frictional pressure for particle type l, $P_{fric,l}$, represents the effect of friction between particles, and this is essential for preventing the particle phase in dense region from packing to an unphysically high level (Houim and Oran, 2016). The relation used here was developed by Johnson and Jackson (1987) and now modified based on the law of partial pressure from kinetic theory,

$$P_{fric,l} = \begin{cases} 0 & \text{if } \alpha_{s,tot} < \alpha_{s,crit} \\ 0.1\dfrac{(\alpha_{s,tot}-\alpha_{s,crit})^2}{(\alpha_{s,max}-\alpha_{s,tot})^5}\alpha_{s,l} & \text{if } \alpha_{s,tot} \geqslant \alpha_{s,crit}, \end{cases} \quad (10)$$

where $\alpha_{s,crit}$ is set to be a critical value of 0.5, and $\alpha_{s,max}$ is the maximum packing limit. For monosized particles, the maximum packing limit for spherical particles are 0.65. For particles containing multiple sizes, the packing limit varies and the correlation developed by Benyahia et al. (2012) and Yu and Standish (1987) is being used.

$$\alpha^{max}_{s,mix} = \min\left\{ \frac{\alpha^{max}_{s,i}}{1-\sum_{j=1}^{i-1}\left(1-\frac{\alpha^{max}_{s,i}}{p_{i,j}}\frac{cx_i}{X_{ij}}\right)-\sum_{j=i+1}^{M}\frac{\alpha^{max}_{s,i}}{p_{i,j}}\frac{cx_i}{X_{ij}}} \right\}, \quad i = 1,2,\ldots,M \quad (11)$$

where

$$cx_i = \frac{\alpha_{s,i}}{\sum_{j=1}^{M}\alpha_{s,j}}, \quad (12)$$

$$X_{i,j} = \begin{cases} \dfrac{1-r_{ij}^2}{2-\alpha^{max}_{s,i}} & \text{if } j < i \\ 1-\dfrac{1-r_{ij}^2}{2-\alpha^{max}_{s,i}} & \text{if } j \geqslant i, \end{cases} \quad (13)$$

$$p_{ij} = \begin{cases} \alpha^{max}_{s,i} + \alpha^{max}_{s,i}(1-\alpha^{max}_{s,i}) \times (1-2.35r_{ij}+1.35r_{ij}^2) & \text{if } r_{ij} < 0.741 \\ \alpha^{max}_{s,i} & \text{if } r_{ij} \geqslant 0.741, \end{cases} \quad (14)$$

and

$$r_{ij} = \begin{cases} \dfrac{d_{p,i}}{d_{p,j}} & \text{if } i \geqslant j \\ \dfrac{d_{p,j}}{d_{p,i}} & \text{if } i < j. \end{cases} \quad (15)$$

Here $\alpha^{\max}_{s,i}$ is the maximum packing limit of individual particle type i and is assumed to be 0.65. As a result, dust mixtures with particle diameters that are closer together have a lower packing limit.

Momentum Source Terms

The source terms in the momentum equations are

$$\boldsymbol{S}^p_g = \sum_{m=1}^{M}\{\boldsymbol{f}_{\mathrm{Drag,gm}} + \boldsymbol{f}_{\mathrm{Lift,gm}}\}, \quad (16)$$

$$\boldsymbol{S}^p_{s,l} = \boldsymbol{f}_{\mathrm{Drag,gl}} + \boldsymbol{f}_{\mathrm{Lift,gl}} + \sum_{\substack{m=1 \\ m\neq l}}^{M}\{\boldsymbol{f}_{\mathrm{Drag,lm}}\} \quad (17)$$

where the quantities $\boldsymbol{f}_{\mathrm{Lift,gm}}$, $\boldsymbol{f}_{\mathrm{Drag,gm}}$ and $\boldsymbol{f}_{\mathrm{Drag,lm}}$ are the lift and drag forces acting between gas phase and the particle type m, and the drag force between particle phase l and m.

The lift force f_{Lift} induced by particle type l acting on gas phase is modeled by the Magnus lift force (Drew and Lahey, 1987),

$$\boldsymbol{f}_{\mathrm{Lift,l}} = C_l\alpha_{s,l}\rho_g(\boldsymbol{v}_{s,l}-\boldsymbol{v}_g)\times(\boldsymbol{\nabla}\times\boldsymbol{v}_g), \quad (18)$$

where C_l is the lift coefficient, which typically takes a value of 0.5. The effect of the Saffman lift force is currently neglected.

The drag force between gas and particle type l, $\boldsymbol{f}_{\text{Drag,gm}}$, is defined by the correlation of Gidaspow (1994),

$$\boldsymbol{f}_{drag,gl} = K_{l,g}(\boldsymbol{v}_{s,l} - \boldsymbol{v}_g), \tag{19}$$

where $K_{l,g}$ is the gas-solid exchange coefficient. The Gidaspow model is used again for $K_{l,g}$, which is a combination of the Wen and Yu model and the Ergun model (Gidaspow, 1994; C.-Y. Wen, 1966; Ergun, 1952),

$$K_{l,g} = \begin{cases} 0.75 C_{d,l} \dfrac{\rho_g \alpha_g \alpha_{s,l} |\boldsymbol{v}_{s,l} - \boldsymbol{v}_g|}{d_{s,l} \alpha_g^{2.65}} & \text{if } \alpha_g \geqslant 0.8 \\ 150 \dfrac{\alpha_{s,l}^2 \mu_g}{\alpha_g d_{s,l}^2} + 1.75 \dfrac{\rho_g \alpha_{s,l} |\boldsymbol{v}_{s,l} - \boldsymbol{v}_g|}{d_{s,l}} & \text{if } \alpha_g < 0.8. \end{cases} \tag{20}$$

Here the drag coefficient $C_{d,l}$ for particle type l is defined as

$$C_{d,l} = \begin{cases} 24(\alpha_g Re_l)^{-1}[1 + 0.15(\alpha_g Re_l)^{0.687}] & \text{if } \alpha_g Re < 1000 \\ 0.44 & \text{if } \alpha_g Re \geqslant 1000, \end{cases} \tag{21}$$

The particle-hindrance force between particle type l and m is a drag-like term between the two corresponding particle types and is defined as Gidaspow (1994),

$$\boldsymbol{f}_{\text{Drag,lm}} = K_{lm}(\boldsymbol{v}_l - \boldsymbol{v}_m) \tag{22}$$

The solid-solid exchange coefficient between particle type l and m is Syamlal (1987),

$$K_{lm} = \frac{\left(\frac{\pi}{2} + C_{fr,lm}\frac{\pi^2}{8}\right)\alpha_l \rho_l \alpha_m \rho_m (d_l + d_m)^2 g_{0,lm}}{2\pi(\rho_l d_l^3 + \rho_m d_m^3)} \times (1 + e_{lm})|\boldsymbol{v}_l - \boldsymbol{v}_m| \tag{23}$$

where e_{lm} is the coefficient of restitution and $C_{fr,lm}$ is the coefficient of friction between particle type l and type m. The friction between different particle types is neglected in the simulation ($C_{fr,lm} = 0$).

Energy Source Terms

The source terms in the energy equations are

$$S_g^E = \sum_{m=1}^{M} \{(\boldsymbol{f}_{\text{Drag,gm}} + \boldsymbol{f}_{\text{Lift,gm}}) \cdot \boldsymbol{v}_g - q_{conv,gm} + \phi_{visc,gm} - \phi_{slip,gm}\}, \tag{24}$$

$$S_{s,l}^{PTE} = -\dot{\gamma}_l - \phi_{visc_gl} + \phi_{slip_{gl}}, \tag{25}$$

$$S_{s,l}^E = q_{conv,gl} + \dot{\gamma}_l, \tag{26}$$

where $-q_{conv,gl}$, $\phi_{visc,\,gm}$, $\dot{\gamma}_l$, and $\phi_{slip,gm}$ are convective heat transfer (Houim and Oran, 2016), dissipation of PTE due to gas-phase viscosity (Gidaspow, 1994), dissipation of PTE due to inelastic particle collisions Lun et al. (1984), and production of PTE due to drag force (Koch and Sangani, 1999).

The heat exchange between particle type m and gas phase, $q_{\text{conv}_{gm}}$, is defined as a function of temperature difference,

$$q_{\text{conv}_{gm}} = h_{\text{mg}}(T_g - T_{s,m}), \tag{27}$$

where the heat exchange coefficient h_{mg} is defined as

$$h_{\text{mg}} = 6\frac{\alpha_{s,m}\lambda_g Nu_m}{d_{s,m}^2}. \tag{28}$$

The Nusselt number, Nu_m, is estimated using the work by Gunn (1978),

$$Nu_m = \left(7 - 10\alpha_g + 5\alpha_g^2\right)\left(1 + 0.7 Re_m^{0.2} Pr_g^{1/3}\right) + \left(1.33 - 2.4\alpha_g + 1.2\alpha_g^2\right) Re_m^{0.7} Pr_g^{1/3}, \tag{29}$$

Table 1
Forces acting on particle type l.

Archimedes force	$-\alpha_{s,l}\nabla p_g$
Intergranular stress	$-\nabla p_{s,l} - \nabla p_{fric,l}$
Drag	$K_{lg}(\boldsymbol{v_g} - \boldsymbol{v_{s,l}})$
Lift	$C_l \alpha_{s,l}\rho_g(\boldsymbol{v_g} - \boldsymbol{v_{s,l}}) \times (\nabla \times \boldsymbol{v_g})$
Particle-hindrance force	$K_{s,lm}(\boldsymbol{v_{s,l}} - \boldsymbol{v_{s,m}})$
Gravitational	$\alpha_{s,l}\rho_{s,l}\boldsymbol{g}$

where

$$\alpha_g = 1 - \sum_{l=1}^{M} \alpha_{s,l}. \tag{30}$$

Here Pr_g is the gas phase Prandtl number, and λ_g is the gas phase thermal conductivity. The Reynolds number related to particle type m is

$$Re_m = \frac{\rho_g |\boldsymbol{v}_{s,m} - \boldsymbol{v}_g| d_{s,m}}{\mu_g}. \tag{31}$$

The transfer of PTE to kinetic energy is represented by $\phi_{\text{visc}_{gm}}$, the viscous damping (Gidaspow, 1994),

$$\phi_{\text{visc}_{gm}} = 3K_{\text{mg}}\theta_{s,m}. \tag{32}$$

The PTE production due to slip between gas and particle type m is Koch and Sangani (1999)

$$\phi_{\text{slip}_{gm}} = \frac{81\alpha_{s,m}\mu_g^2}{g_0 d_{s,m}^3 \rho_{s,m}\sqrt{\pi}} \frac{\rho_s \theta_{s,m}^{3/2}}{d_{s,m}}. \tag{33}$$

The dissipation of PTE due to collisions between particles is given by Lun et al. (1984),

$$\dot{\gamma}_l = \frac{12(1 - e^2) g_{0,ll} \alpha_{s,l}^2}{\sqrt{\pi}} \frac{\rho_{s,l} \theta_{s,l}^{3/2}}{d_{s,l}}. \tag{34}$$

Governing Forces

From the above equations, we can identify six governing forces responsible for the granular motion. Evaluating these forces helps to understand the dust-lifting mechanism. Table 1 summarizes the six forces that act on particle type l. The lift and drag forces result from the velocity difference between the particles and the gas. The Archimedes force is due to the gas-phase pressure pushing on the particles. The intergranular stress corresponds to the collisional and frictional effect of the particles. The particle-hindrance force is a drag-like force between the two particle types. Gravity is not important in the time scale of our simulations, so it is exempted from discussion.

2.2. Numerical model

A full description of the numerical algorithm can be found in Houim and Oran (2016) and in Lai et al. (2018). An operator-splitting algorithm is used to integrate the hyperbolic terms and the source terms. The hyperbolic terms are solved using a high-order Godunov-based scheme (Houim and Kuo, 2011), where the primitive variables are implemented using a MUSCL method with a third order parabolic reconstruction. A total variation diminishing (TVD) scheme with minmod slope limiter is also adopted to reduce small oscillations near discontinuities. A modified HLLC method,which returns primitive variables directly, is used to solve for the gas-phase flux. The granular flux is computed using a modified AUSM+ -up method to increase dissipation in highly packed regions. The lifting Magnus force is discretized using a first-order backward differencing scheme. The Strang operator (Houim and Oran, 2016) further splits the source terms into two parts: (1) drag, particle-hindrance effect, and convective heat transfer and

(2) pseudothermal energy production and dissipation. These source terms are integrated analytically into the solutions (Pelanti and LeVeque, 2006). The solution algorithm uses a third-order Runge-Kutta scheme (Spiteri and Ruuth, 2002) for time advancement. Adaptive mesh refinement is implemented through the Boxlib library (Bell et al., 2012). The simulations shown below are performed with 5 levels of refinment, which gives a minimum cell size of 156 µm.

3. Results

From early studies of a shock passing over a single dust layer containing different particle types, we find that the different types of particles in the mixture separate into different regions. Larger particles are lifted higher than smaller particles. This result leads to the following question: *What is the consequence of placing a layer of smaller particles on top of a layer of larger particles?* This questions is addressed in Section 3.1. Section 3.2 investigates the dispersion of stratified coal- and rock-dust layers in actual coal mine conditions. In particular, we ask: *How thick does an inert dust layer sitting on a layer of coal dust have to be to suppress a secondary explosion?*

3.1. The effect of particle size on dispersion of a stratified dust layer

3.1.1. Shock lifting 10-µm particles on 80-µm particles

The computed results of a shock passing over two layers of dust, where the top layer contains particles with a diameter of 10 µm and the bottom layer contains particles with a diameter of 80 µm are shown in Fig. 2. Here, both particle types have the same density, ρ_s =1300 kg/m^3. The bottom and top layers have thicknesses of $h_1 = 10$ mm and $h_2 = 2.7$ mm, respectively. The top two images in Fig. 2 show the particle volume fractions for the top and the bottom dust layers ($d_{s,2}$ =10 µm and $d_{s,2}$ =80 µm). The third image demonstrates the location of each type of particles in the dust mixture. Particle volume fractions below 0.005% are not shown. The bottom image shows the gas pressure contour with the gas-phase streamlines (shock-attached frame). Note that a very small region of mixed particle types sits between the two layers in the region to the right of the vertical line marked “Gas Shock” in Fig. 2. Besides being a more realistic representation of the physics, this also eliminates a sharp discontinuity in the initial conditions.

The top three figures show that far enough behind the leading shock, the larger particles ($d_{s,2}$ =80 µm) placed in the lower layer are lifted much higher than the smaller particles that comprise the upper layer. Starting at the leading shock and moving upstream, the dust-lifting process can be divided into two stages: I) Compressing and Mixing stage, and II) Dispersing stage. In stage I, the top layer is pushed into the bottom layer through gas-phase pressure and drag forces, so that the gas flow streamlines (lowest frame in Fig. 2) turn downwards to follow the compressing dust layer. During this stage, the two layers are mixing with each other, forming a region where both types of particles coexist.

Then, in stage II, the particles in the mixed region begin to be lifted. The dispersing mechanism is similar to what we found in our earlier studies of two types of particles mixed in a single dust layer. The larger particles are lifted to a higher level than smaller particles due to the differences in the Magnus lifting force and drag force (Lai et al., 2018). Note that during this dispersion process, both “mixing” and “unmixing” of the two types of particles are observed.

We also investigated the effect of Mach number on dust dispersion for the test case shown above. The simulation results with three different Mach numbers (Mach = 1.2, 1.4, and 1.6) are shown in Fig. 3. The particle volume fraction contour show that particles

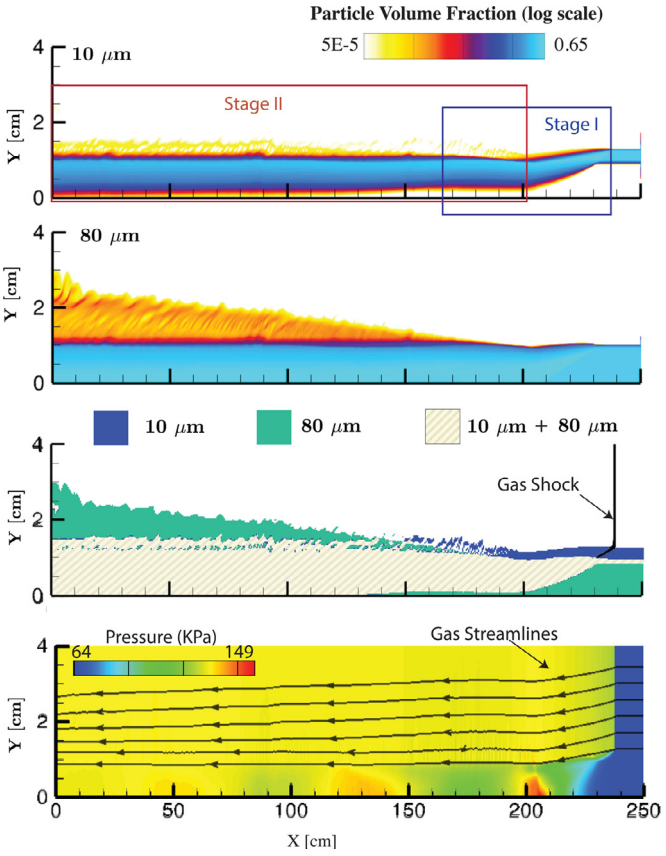

Fig. 2. Simulation results of a Mach 1.4 shock passing over two layers of dust, where the top layer contains particles with a diameter of 10 µm and the bottom layer contains particles with a diameter of 80 µm. The top two images show the particle volume fraction contours of the 10 µm and 80 µm particles. The third image shows the location of each type of particle. The bottom image shows the gas pressure contour with the gas phase streamlines (shock-attached frame) indicated.

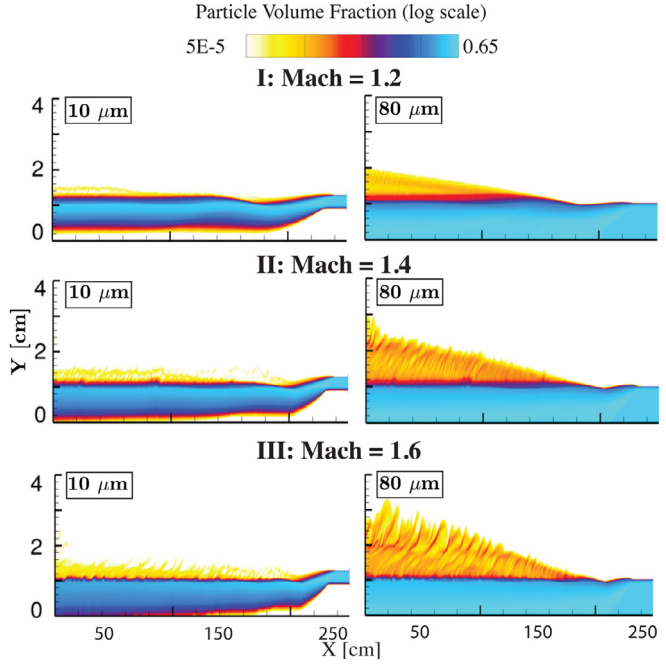

Fig. 3. Particle volume fraction contours of shock (Mach= 1.2, 1.4, and 1.6) passing over two dust layers. The top layer contains particles with a diameter of 10 µm, and the bottom layer contains particles with a diameter of 80 µm.

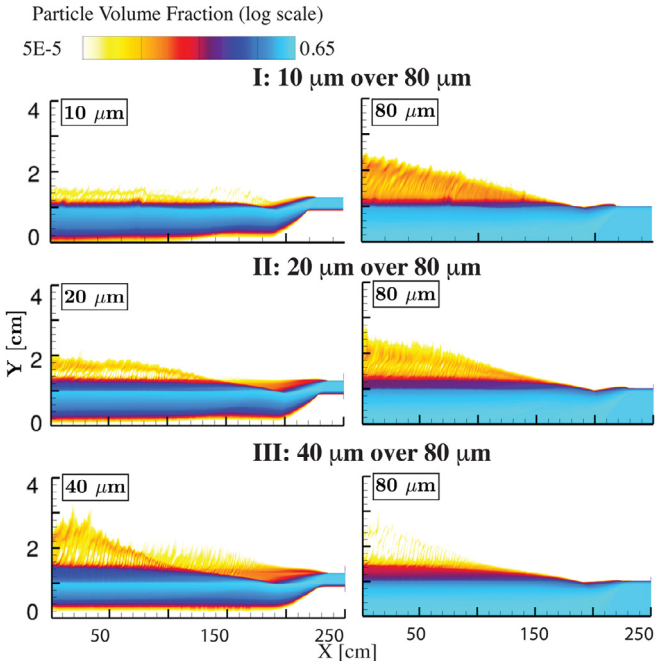

Fig. 4. Computed particle volume fractions of the top and bottom layer for the three test cases. The top layer contains particles with a diameter of 10, 20, and 40 μm, respectively. The bottom layer contains particles with a 80-μm diameter.

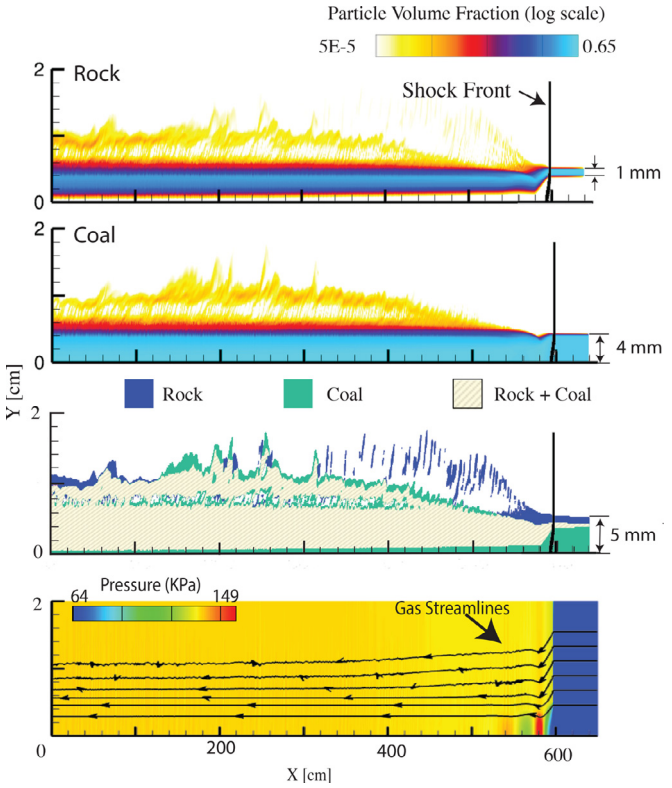

Fig. 6. Simulation results of a Mach 1.4 shock passing over 1-mm rock layer on top of 4-mm coal layer. The top two image show the particle volume fraction contour of the rock and coal particles. The bottom image indicates the location of each type of particle.

are lifted higher as the Mach number is increased. The lifting behavior of the two dust layers remain qualitatively the same regardless of the Mach number, and the larger particles from the bottom layer are lifted higher than the smaller particles from the top layer in all the three cases shown here.

3.1.2. *Increased particle size in the top layer* ($d_{s,2}$=10, 20, and 40 μm)

Here, the effect of the particle size in the top layer is explored. Three test cases with particle of d_s = 10, 20, and 40 μm in the top layer are considered, where d_s is the particle diameter. The particle diameter in the bottom layer remains at 80 μm. All of the other input parameters are the same as described in Section 3.1.1. The particle volume fractions and the edge of the dispersed dust ($\alpha_{s,edge} = 0.005\%$) for both layers in the three test cases are shown in Figs. 4 and 5.

Figs. 4 and 5 indicate that the top layer with smaller particles is lifted higher as the size of the small particles increases. The edge of the bottom layer ($d_{s,1}$ =80 μm) shown in Fig. 5 is lifted to a similar height in all three cases, with Case III slightly lower than Case I. The particle volume fractions of the bottom layer shown in Fig. 4, however, indicate that the bottom layer becomes much less dispersed as the particle size in the top layer increases. We find that the larger particles from the lower layer are lifted higher than the smaller particles from the upper layer in Cases I and II. This conclusion is then challenged in Case III as we further increase the particle size in the top layer, and the larger particles in the lower layer ($d_{s,1}$ =80 μm) are now less dispersed than the smaller particles ($d_{s,2}$ =40 μm) in the top layer.

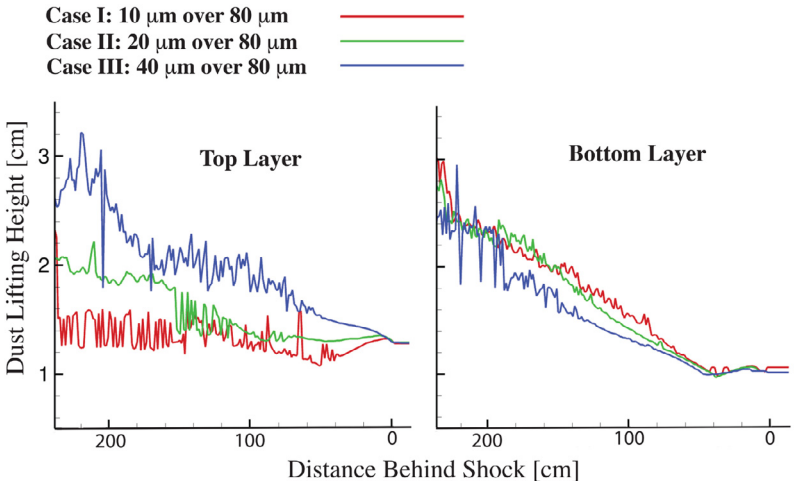

Fig. 5. Computed dust-lifting height for the top layer (left), and the bottom layer (right) for the three test cases. The edge of the dust layer is defined as $\alpha_s = 0.005\%$.

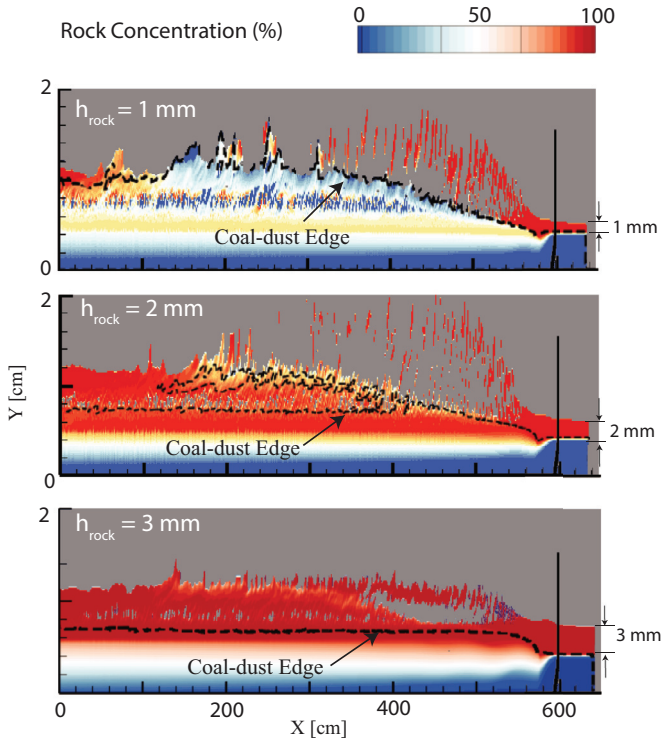

Fig. 7. Computed rock concentrations for rock-layer thicknesses of $h_2 = 1$, 2, and 3 mm. The location of the dispersed coal dust edge and the propagating shock wave are indicated. The coal-dust layer remains at 4 mm for all cases.

These results show that the dispersion of the stratified dust layer is largely dependent on the size difference between the two types of particles. Larger particles from the bottom layer are lifted higher than smaller particles from the top layer only when the two types of particle have a relatively large size difference.

3.2. Rock dusting in coal mines

In this section, the effect of rock dusting in preventing and reducing the coal-dust dispersion and explosion is explored. Here, the rock dust has a diameter of 15 µm and a density of 2680 kg/m^3, and the coal dust has a diameter of 30 µm and a density of 1330 kg/m^3. Test cases with smaller dust-layer thicknessses are considered. (These parameters we provided courtesy of Marcia Harris and Michael Sapko of NIOSH).

3.2.1. Dispersion of 1 mm rock dust on 4 mm coal dust

The computed results of a shock passing over a layer of 1 mm rock dust placed on top of a layer of 4 mm coal dust is shown in Fig. 6. The top two images in Fig. 6 show the particle volume fractions for the coal and rock dust on a log scale. The bottom image in Fig. 6 indicates the location of coal and rock particles. Here, particles with a volume fraction less than 0.005% are not shown. Fig. 6 shows that the coal and rock particles are mixed with each other in most of the dispersed region, and there is no apparent separation between the two types of particles. In the area closer to the moving shock wave (400 ∼ 600 cm), however, the entrained dust is primarily rock dust (blue region). This is because dust lifting from the top layer begins immediately behind the propagating shock wave, and there is a delay in dust lifting from the bottom layer. In the rest of the region (0 ∼ 400 cm), the coal particles are lifted slightly higher than the rock particles, even though they were initially placed in the lower level. This result is consistent with earlier results that larger and lighter particles are lifted higher than smaller and heavier particles (Lai et al., 2018).

3.2.2. The effect of rock-Layer height on dust dispersion

Here, the effect of the rock-layer (upper layer) thickness on dispersion of a 4-mm coal layer (lower layer) is examined. Rock-layer heights of $h_2 = 1$, 2, and 3 mm are considered. The computed rock-dust concentrations for all the three cases are shown in Fig. 7 with the edge of the coal particles indicated. Here, blue indicates a coal-dominate region, while red indicates a rock-dominate region. The results show that the coal dust from the lower layer rises more slowly with increasing rock-layer thickness in the upper layer. In addition, the rock dust in the upper layer also becomes less dispersed with increasing rock-layer thickness. In the first case ($h_2 =$ 1 mm), rock particles have a concentration close to or less than 50% in most of the dispersed region and coal particles are lifted to a similar level as the rock particles. In the second case ($h_2 = 2$ mm), the rock particles are more dispersed than the coal particles, and rock particles dominate in the dispersed region with a concentration ranging from 60% to 100%. In the last case ($h_2 = 3$ mm), the dispersed dust consists of primarily rock particles and the coal dust is hardly lifted. In this case, the 80% total incombustible content (TIC) requirement is achieved in most of the dispersed region.

3.2.3. Rock dusting: Dispersion of three dust layers

As the mining face advances, the coal particles generated fall on top of the applied rock dust, forming a system containing multiple stratified rock and coal layers. Here, the case of a Mach 1.4 shock passing over three dust layers is examined. The initial configuration is shown in Fig. 8, where the top and bottom layers contain coal particles and the middle layer contains rock particles. The three layers have thicknesses of $h_1 = 4$, $h_2 = 3$, and $h_3 = 1$ mm. The other parameters remain the same as the previous calculations.

The computed particle volume fractions for the rock and coal particles and the rock concentration are shown in Fig. 9. These figures indicate that the coal dust rises more rapidly than the rock dust, and the rock particles underneath do not suppress dispersion of the coal-dust layer on top of it. In fact, only particles from the top part of the dust layer are lifted. The coal particles from the

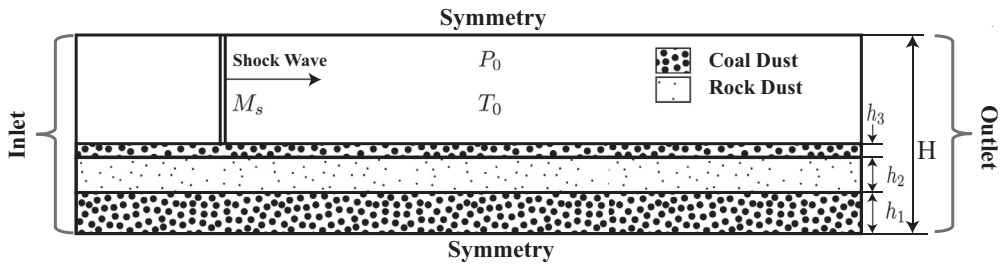

Fig. 8. Schematic diagram of the initial conditions for the two-dimensional simulations where a shock of stregth M_s travels over three dust layers. The top and the bottom layers consist of coal particles, and the middle layer consists of rock particles.

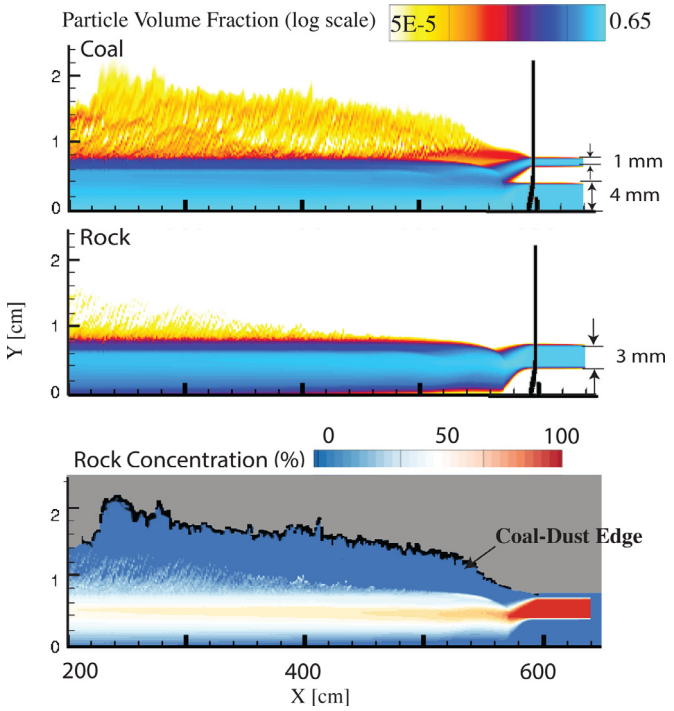

Fig. 9. Computed particle volume fractions of coal and rock dust and rock concentration for the case of a shock passing over three dust layers. The location of the shock wave and the edge of the dispersed coal dust are indicated in the rock concentration contour.

bottom layer (0 ~ 4 mm) are barely dispersed. The rock concentration suggests that coal particles dominate in the dispersed region.

4. Discussion

Thus the simulations have shown us that when there is a layer of large particles under a layer of small particles, the large particles may be lifted higher than the small particles. This interesting result is not always true, and can vary depending on the relative sizes of the particles and the thickness of the layers. Now we examine why this is happens.

4.1. Analysis of the effect of particle size

First, we examined the case where a 2.7-mm thick layer containing particles with a 10-μm diameter is placed on top of a 10-mm layer containing particles with a 80-μm diameter. To help understand why the bottom layer is much more dispersed than the top layer, the governing forces (Table I) acting on each particle type are evaluated. Fig. 10 shows the net vertical acceleration and the accelerations due to lift, drag, particle-hindrance force, intergranular stress, and Archimedes force for the top and the bottom layer in the region between $X = 100$ to 240 cm. The particle streamlines in the shock reference frame are overlaid on the net acceleration for each layer.

Initially (just behind the shock), the surface of the top dust layer is lifted slightly due to the positive lift and intergranular stress forces. This minor lifting effect is soon overcome through the negative Archimedes and drag force from the gas flow acting on the top layer, and no apparent lifting is observed in the region just behind the shock (200 ~ 240 cm). These compression forces push the top layer into the bottom layer and form a mixed region (overlapping area in the third image in Fig. 2). During this compression and mixing process, particles from the top layer develop a larger downward vertical velocity (sharper slope for the particle streamlines) than particles in the bottom layer. Therefore, the particle hindrance force produces a negative force on the bottom layer while exerting positive force on the top layer. This effect reduces the velocity difference between the larger and the smaller particles, and this, in turn, slows down the mixing process.

At later stages, the dispersion of particles in the mixed region is enhanced by the interaction of the reflected compaction wave (marked in Fig. 10) and the surface of the compacted dust layer (Houim et al., 2016). Dispersion of particles from both top and bottom layers are observed, with the 80-μm particles in the bottom layer lifted higher than the 10-μm particles from top layer. During the lifting process, the bottom layer experiences a negative particle-hindrance force from the top layer. This effect, however, is not very significant in the dispersed region, since the top layer ($d_{s,2} = 10$ μm) is hardly lifted.

The dust-lifting process in the mixed region is similar to what was seen in earlier studies (Lai et al., 2018), where a shock passed through a layer of dust containing two types of uniformly mixed particles. These prior results suggested that larger particles are lifted higher than smaller particles mainly due to the differences in lift force and drag forces. This is also true for the two-layer case simulated here, since the dispersion occurs after the two dust layers mix with each other. Fig. 11 shows the accelerations due to lift and drag forces acting on the two particle types along a vertical line located at X = 120 cm. Similarly, we find that the 80 μm particles have a larger positive lift force that pushes them upwards and a smaller negative drag force pushing them downwards than those acting on the 10 μm particles.

Test cases with systematically increased particle size in the top layer ($d_{s,2}$ =10, 20, and 40 μm) and fixed particle size in the bottom layer ($d_{s,1}$ =80 μm) suggest that the top layer works more effectively in suppressing lifting in the bottom layer when the two types of particles are closer in size. The drag force, which is inversely proportional to the particle size, pushes on the top layer. This force is smaller for case III ($d_{s,2}$ =40 μm) than for case I ($d_{s,2}$ =10 μm) in Fig. 4. Therefore, the mixing and compression effects become weaker for cases where the top layer contains larger particles. In addition, a smaller size difference indicates a smaller solid packing limit ($\alpha_{s,max}$) and lower particle concentrations in the mixed region. As a result, the mixed particle region in case III in Fig. 4 contains fewer larger particles from the bottom layer than in case I, and the smaller particle on top of the larger particles now effectively suppress lifting of the larger particles. When the particle size in the top layer is further increased to approximately 80 μm, the bottom layer would be even more suppressed.

4.2. Analysis of rock- and coal-Dust dispersion

In Section 3.2, we explored dust dispersion behind a moving shock where a thin layer of rock dust is applied on top of a thicker layer of coal dust. Here, the rock particles are smaller and denser than coal particles. According to our previous conclusions, coal particles are lifted higher by a shock than rock particles.

The results shown in Figs. 6 and 7 suggest that the coal-dust layer rises more rapidly with decreasing rock-dust thickness. In fact, we find that when the top layer is very thin, particles from both layers are dispersed. This occurs regardless of the density or size ratio of the dust particles between the upper and lower layers of dust. With more rock dust applied on top of the coal-dust layer, the positive intergranular stress (pressure-like effect on the granular particles), which initiates the lifting behavior within the coal dust layer decreases, since the coal dust now has a lower granular energy due to interparticle collisions and friction. In addition, with a thicker rock-layer applied, the dispersed coal particles experience a larger negative particle hindrance force, which suppresses the lifting.

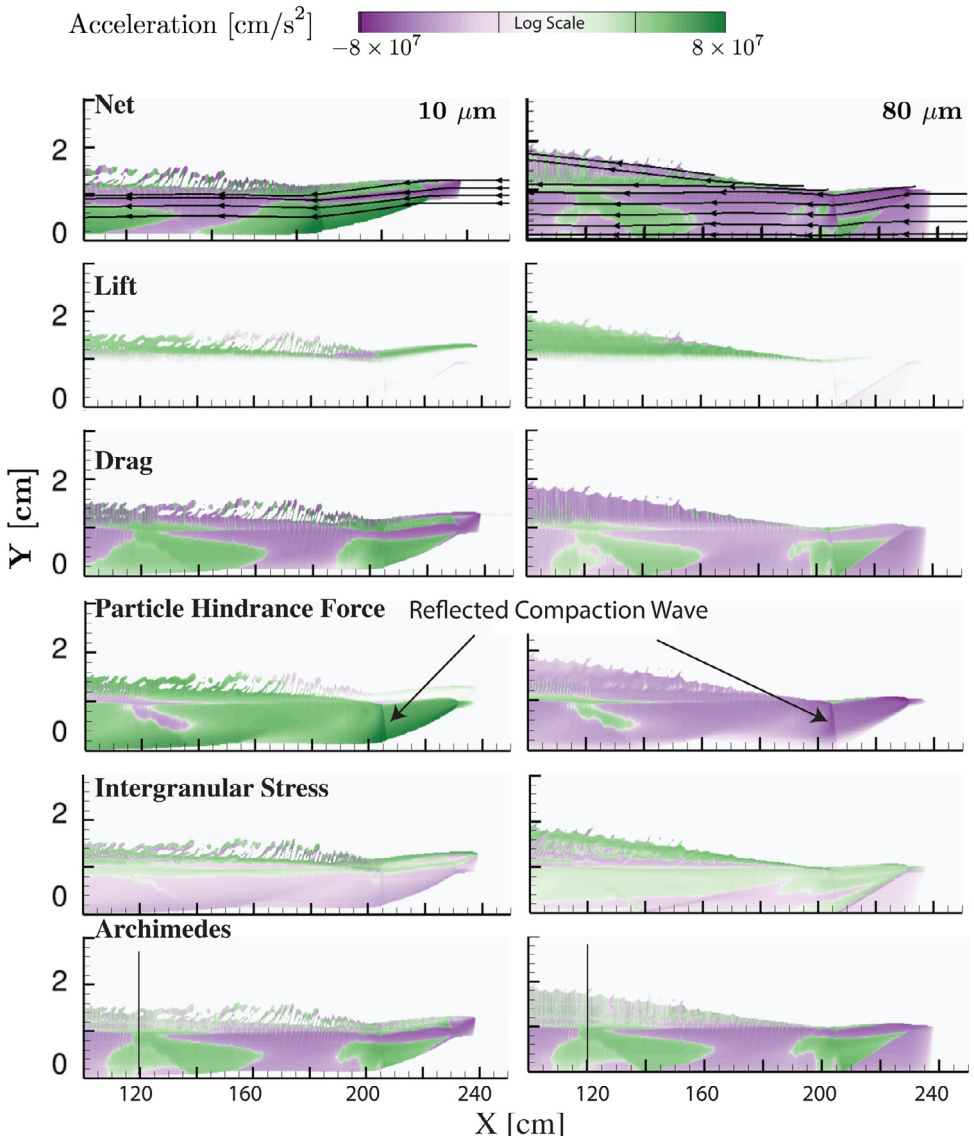

Fig. 10. Vertical accelerations and accelerations due to drag, Archimedes force, lift, particle hindrance force, and intergranular stress for both types of particles. Forces have been normalized by $\alpha_s \rho_s$. The particle streamlines, and the location of the reflected compaction wave are indicated.

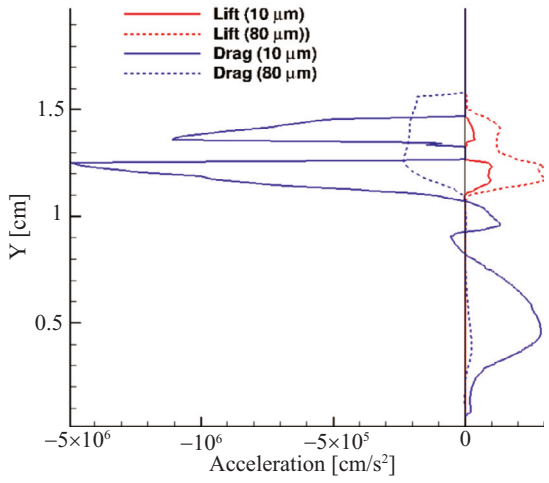

Fig. 11. Accelerations due to lift and drag forces acting on the two types of particles along the vertical line at X = 120 cm.

During the mining operation, more coal particles are generated and form another coal-dust layer on top of the applied rock-dust layer. Thus there are three layers: coal on top of dust on top of coal. Similarly, the coal particles from the top layer are pushed into the rock and coal layer underneath. In fact, the two coal-dust layers mix with each other after the compression and mixing stage. The coal dust from the upper layer, which is larger in size and smaller in density, rises quickly just behind the moving shock wave and before the mixing stage begins. The thick layer of rock dust underneath does not mix with the coal dust generated during the mining process, and therefore fails to inert explosions when the coal-dust layer becomes thick enough. This rapid dispersion of coal dust suggests that it is beneficial to apply rock dust regularly during the mining operation.

Ideally, to keep the coal dust from rising and igniting, we need two conditions to be fulfilled: rock particles from the upper layer should suppress the coal particles from the bottom layer, and the rock concentration in the dispersed region should be greater than 80% (Luo et al., 2017). Based on the results discussed above, it is recommended that the rock-dust particles be larger (or close) than the coal-dust particles to ensure that the rock particles are

dispersed to a higher level than the coal particles. A relatively thick rock-dust layer is necessary to meet the 80% TIC limit. In addition, we want to ensure that at least a portion of the rock dust travels in lockstep with the coal dust during the dispersion process. This suggests that a size distribution of rock dust is recommended.

4.3. Future work

The dispersion of multiple dust layers are complex processes that depend on many factors. Here, we focused the effect of particle size and dust-layer thickness. Other parameters, such as the shock wave Mach number, coefficient of restitution, and initial packing could also be very important. In addition, the representation of lift force (now modelled as the Magnus force) in our model may not accurately simulate the dust-lifting process. The effect of other lift forces such as Saffman force needs to be evaluated. The sensitivity of the solution to some of the parameters that describe the contributing forces can also be studied. (For example, the effects of frictional pressure ($P_{fric,l}$), collisional pressure ($P_{c,lm}$), solid-solid exchange coefficient (S_{coef}) (Lai et al., 2018), and the Magnus and Saffman lift coefficients on the simulation results can be explored.) More importantly, developing a general correlation that could be used to predict the dust dispersal height as a function of these parameters (particle size, dust-layer thickness, Mach number, etc.) would be extremely useful to optimize the selection of rock-dust properties applied in a coal mine to prevent explosions.

5. Conclusions

In this paper, the effects of particle size and dust layer thickness on dispersion of stratified layers of dust behind a moving shock wave have been examined through numerical simulations using a mutifluid granular model.

It has been shown that when there is a layer of large particles under a layer of small particles, the large particles may be lifted higher than the small particles, when the two types of particles have relatively large size difference. With increasing particle size in the top layer, the compaction and mixing process becomes less significant, and the top layer becomes more dispersed while the bottom layer is less dispersed. In terms of rock and coal dispersal in actual coal mine conditions, a relatively thick (3 mm) rock-dust layer is needed on top of coal-dust layer to meet the 80% total incombustible content requirement. We also find that even a very thin layer of coal dust on top of an inert dust layer is sufficient to produce a reactive particle cloud when dispersed by a shock wave. This indicates the need to apply the rock dust continually during the mining operations. Ideally, we want the rock-dust particles to be larger (or close) than the coal-dust particles, so that any dispersed coal dust is well mixed with inert dust.

Acknowledgments

This work was supported in part by NIOSH Grant No. 200-2015-64091 and in part by the University of Maryland through Minta Martin Endowment Funds in the Department of Aerospace Engineering, and through the Glenn L. Martin Institute Chaired Professorship and the A. James Clark Distinguished Professorship at the A. James Clark School of Engineering. The authors would like to thank Mike Spako and Marcia Harris for their valuable comments and suggestions. The authors acknowledge the University of Maryland supercomputing resources (http://www.glue.umd.edu/hpcc) made available in conducting the research reported in this paper.

References

Bell, J., Almgren, A., Beckner, V., Day, M., Lijewski, M., Nonaka, A., Zhang, W., 2012. Boxlib user?s guide. github. com/BoxLib-Codes/BoxLib.
Benyahia, S., Syamlal, M., O?Brien, T., 2012. Summary of mfix equations 2012-1. From URL https://mfix.netl.doe.gov/documentation/MFIXEquations2012-1.pdf.
Borisov, A., Lyubimov, A., Kogarko, S., Kozenko, V., 1967. Instability of the surface of a granular medium behind sliding shock and detonation waves. Combust. Explos. Shock Waves 3 (1), 95–97.
C.-Y. Wen, Y.Y., 1966. Mechanics of fluidization. Chem. Eng. Progr. Sympos. Ser. 62, 100–111.
Chowdhury, A., Johnston, H.G., Mashuga, C.V., Mannan, M.S., Petersen, E.L., 2018. Effect of particle size and polydispersity on dust entrainment behind a moving shock wave. Exp. Thermal Fluid Sci. 93, 1–10.
Chowdhury, A.Y., Johnston, H.G., Marks, B., Mannan, M.S., Petersen, E.L., 2015. Effect of shock strength on dust entrainment behind a moving shock wave. J. Loss Prevent. Process Ind. 36, 203–213.
Drew, D., Lahey, R., 1987. The virtual mass and lift force on a sphere in rotating and straining inviscid flow. Int. J. Multiphase Flow 13 (1), 113–121.
Ergun, S., 1952. Fluid flow through packed columns. Chem. Eng. Prog. 48, 89–94.
Fletcher, B., 1976. The interaction of a shock with a dust deposit. J. Phys. D 9 (2), 197.
Gerrard, J., 1963. An experimental investigation of the initial stages of the dispersion of dust by shock waves. Brit. J. Appl. Phys. 14 (4), 186.
Gidaspow, D., 1994. Multiphase Flow and Fluidization: Continuum and Kinetic Theory Descriptions. Academic press.
Gunn, D., 1978. Transfer of heat or mass to particles in fixed and fluidised beds. Int. J. Heat Mass Transf. 21 (4), 467–476.
Houim, R., Ugarte, O., Lai, S., Oran, E., 2016. Mechanisms of Dust Scouring Behind Shock Waves. In: Proceedings of the 11th International Symposium on Hazards, Prevention, and Mitigation of Industrial Explosions, pp. 188–202.
Houim, R.W., Kuo, K.K., 2011. A low-dissipation and time-accurate method for compressible multi-component flow with variable specific heat ratios. J. Comput. Phys. 230 (23), 8527–8553.
Houim, R.W., Oran, E.S., 2016. A multiphase model for compressible granular–gaseous flows: formulation and initial tests. J. Fluid Mech. 789, 166–220.
Huilin, L., Yurong, H., Gidaspow, D., 2003. Hydrodynamic modelling of binary mixture in a gas bubbling fluidized bed using the kinetic theory of granular flow. Chem. Eng. Sci. 58 (7), 1197–1205.
Hwang, C., 1986. Initial stages of the interaction of a shock wave with a dust deposit. Int.J.Multiphase Flow 12 (4), 655–666.
Johnson, P.C., Jackson, R., 1987. Frictional–collisional constitutive relations for granular materials, with application to plane shearing. J. Fluid Mech. 176, 67–93.
Koch, D.L., Sangani, A.S., 1999. Particle pressure and marginal stability limits for a homogeneous monodisperse gas-fluidized bed: kinetic theory and numerical simulations. J. Fluid Mech. 400, 229–263.
Lai, S., Houim, R.W., Oran, E.S., 2018. Effects of particle size and density on dust dispersion behind a moving shock. Phys. Rev. Fluids 3 (6), 064306.
Lun, C., Savage, S.B., Jeffrey, D., Chepurniy, N., 1984. Kinetic theories for granular flow: inelastic particles in couette flow and slightly inelastic particles in a general flowfield. J.Fluid Mech. 140, 223–256.
Luo, Y., Wang, D., Cheng, J., 2017. Effects of rock dusting in preventing and reducing intensity of coal mine explosions. Int. J. Coal Sci.Technol. 4 (2), 102–109.
Man, C., Teacoach, K., 2009. How does limestone rock dust prevent coal dust explosions in coal mines? Min. Eng. 61 (9), 69.
Pelanti, M., LeVeque, R.J., 2006. High-resolution finite volume methods for dusty gas jets and plumes. SIAM J. Sci. Comput. 28 (4), 1335–1360.
Spiteri, R.J., Ruuth, S.J., 2002. A new class of optimal high-order strong-stability-preserving time discretization methods. SIAM J. Numer. Anal. 40 (2), 469–491.
Suzuki, T., Adachi, T., 1984. The Effects of Particle Size on Shock Wave-Dust Deposit Interaction. In: 14th Space Technology and Science Symposium, pp. 483–490.
Syamlal, M., 1987. The Particle-Particle Drag Term in a Multiparticle Mmodel of Fluidization. Technical Report. EG and G Washington Analytical Services Center, Inc., Morgantown, WV (USA).
Ugarte, O., Houim, R., Oran, E., 2017. Examination of the forces controlling dust dispersion by shock waves. Phys. Rev. Fluids 2 (7), 074304.
Yu, A., Standish, N., 1987. Porosity calculations of multi-component mixtures of spherical particles. Powder Technol. 52 (3), 233–241.
Zhu, C., Lin, B., Jiang, B., Liu, Q., Hong, Y.-D., 2012. Dust lifting behind a shock wave: analysis based on the ee method. J. China Univ. Mini. Technol. 5, 008.